Precise excitation-inhibition balance controls gain and timing in the hippocampus

Aanchal Bhatia[1], Sahil Moza[1], Upinder S. Bhalla[*]

National Centre for Biological Sciences, Tata Institute of Fundamental Research, Bellary Road, Bangalore 560065 India

[1]Equal contribution

[*] Corresponding author (bhalla@ncbs.res.in)

ABSTRACT

Balanced excitation and inhibition contributes to clamping excitability, input gating, and dynamic range expansion in many brain circuits. However, it is unknown if the balancing mechanism operates at the level of networks, ensembles or individual projections. We optogenetically stimulated hippocampal CA3 neurons in hundreds of different combinations, and monitored CA1 neuron responses in mouse brain slices. We observed that all arbitrary input combinations from CA3, from tens of synapses to the order of single synapses, elicited excitation followed by tightly proportional inhibition. CA1 neurons summed these complementary inputs and exhibited gain control in the form of subthreshold divisive normalization (SDN). Biophysically, SDN emerged because inhibitory onset advanced toward excitatory onset with increasing input strength. This caused clipping of peak amplitudes and faster peak times, resulting in shared input information

coding between the two. Our results suggest that SDN may be a general gain and timing control mechanism in balanced feedforward networks.

INTRODUCTION

Excitation and Inhibition (E and I) are normally closely balanced throughout the brain[1–4]. This EI balance implies that the ratio of excitatory and inhibitory inputs to a cell remains invariant[5]. Clinically, imbalance of excitation and inhibition is linked with several pathologies, including epilepsy, autism spectrum disorders and schizophrenia[6]. Computationally, individual neurons integrate incoming excitation and inhibition to perform subtraction, division, and normalization of inputs[7,8]. This has functional consequences such as preventing runaway excitation, gain control[9], maximizing sensitivity to various stimuli, and attentional modulation[10].

Strong EI correlations have been seen in several brain regions in response to various stimuli, for instance, series of tones in auditory cortex[2,11,12], whisker stimulation in somatosensory cortex[13], during cortical up states in vitro[14] and in vivo[15], during gamma oscillations in vitro and in vivo[4], and during spontaneous activity[3]. However, the presynaptic origin of balance is not well understood. It remains to be established if this balance results from a single presynaptic population, summation of multiple presynaptic populations, or from complex temporal dynamics of multiple presynaptic layers.

In the context of temporal dynamics and presynaptic granularity two key classifications of EI balance have been theoretically explored: ‘loose’ vs. ‘tight’[16] (in the time domain), and ‘global’ vs. ‘detailed’[17] (in the domain of granularity of input combinations). Neurons in loosely balanced EI networks are balanced only on slow timescales (~100 ms), leading to chaotic dynamics and unreliable spike times[16,18,19]. Conversely, neurons in tightly balanced EI networks receive input

balanced at fast (<10 ms) timescales, and have reproducible spike times, making them good temporal coders[16].

In the domain of granularity of input, there is a distinction between global and detailed balance. Global balance implies that neurons exhibit EI balance on average (for example, responses averaged over sensory inputs), whereas detailed balance implies that all subsets of input neurons elicit balanced responses[17]. Based on the latter, neurons can effectively gate several inputs by reporting I/E ratio imbalances on arbitrary subsets of inputs, constituting an instantaneous information channel[17,20]. When detailed balance is also temporally tight, it is referred to as precise balance[21].

In this study we address two key open questions in the field. First, does EI balance arise even from single presynaptic networks, and if so, at what granularity of network subsets do postsynaptic cells experience balanced excitation and inhibition? Second, how do excitation and inhibition integrate to encode and communicate information at the postsynaptic neuron? We addressed these questions *in vitro*, to isolate the hippocampal network from background activity and to precisely control the stimulus. We stimulated channelrhodopsin-2 (ChR2) expressing CA3 neurons with tens to hundreds of optical patterns, and measured responses in CA1. We found that all randomly chosen subsets of CA3 neurons provided tightly coupled excitatory and feedforward inhibitory inputs to CA1 cells, thus, for the first time demonstrating precise balance[21] in the brain. We further examined the arithmetic form of the integration performed by this tightly balanced feedforward inhibitory network. Surprisingly, we found that integration of excitation and feedforward inhibition leads to divisive normalization at subthreshold potentials. Moreover, this novel gain control operation encodes input information in both amplitude and timing of the CA1 response.

RESULTS

Patterned optical stimuli in CA3 elicit subthreshold responses in CA1

To provide a wide range of non-overlapping stimuli, we projected patterned optical stimuli onto channelrhodopsin-2 (ChR2) expressing CA3 neurons in acute hippocampal slices. We used CA3-cre mice to achieve CA3-specific localization of ChR2 upon injection of a Lox-ChR2 virus (**Fig. 1a, Methods**). We used a Digital Micromirror Device (DMD) projector (**Methods**, **Supplementary Fig. 1**) to generate spatiotemporal optical patterns in the form of a grid of several 16um x 16um squares, each square approximating the size of a CA3 soma[22] (**Fig. 1d**). This grid was centered at the CA3 cell body layer, and extended to the dendritic layer (**Fig. 1a**). Each optical pattern consisted of 1 to 9 such randomly chosen grid squares, presented to CA3 cells as stimulus, at an inter-stimulus interval of 3 seconds (**Fig. 1a, 1d**, **Methods**). In a typical experiment, several randomly chosen stimulus patterns with different number of input squares were delivered to CA3, in 3 successive repeats. We first characterized how CA3 responded to the grid stimulation (**Fig. 1b,e,f,g**). We confirmed that CA3 neurons fired reliably with a <2ms jitter, calculated as the standard deviation of the time of first spike (**Fig. 1f**) (n = 8 CA3 cells, inputs = 52, median = 0.44 ms, N = 1 to 9 squares). No desensitization occurred during the timeframe of an experiment, and the probability of spiking remained constant between the 3 repeats (**Fig. 1g**) (n = 7 CA3 cells, N = 1 to 9 squares). Thus, we could stimulate CA3 with hundreds of distinct optical stimuli in each experiment.

We then recorded postsynaptic potentials (PSPs) evoked at patched CA1 neurons while optically stimulating CA3 cells (**Fig. 1c,h,i,j**). A wide range of stimulus positions in CA3 excited CA1 neurons (**Fig. 1c**). Stimulation of CA3 elicited excitation and feedforward inhibition at CA1 (**Fig. 1a**, **Supplementary Fig. 3**). Most stimuli elicited subthreshold responses (N = 1 to 9

94 squares). Action potentials occurred in only 0.98% of trials (18,668 trials, from 38 cells, N = 1 to
95 9 squares). This helped rule out any significant feedback inhibition from CA1 interneurons for all
96 our experiments. Restriction of ChR2 to CA3 pyramidal cells, coupled with the fact that ~99% of
97 all recorded CA1 responses were subthreshold, ensured that the recorded inhibition was largely
98 feedforward (disynaptic)(**Fig. 1a**). Responses to the same 1-square stimulus were consistent,
99 84.74% responses showed less than 0.5 variance by mean (695 stimuli, 3 repeats each, n = 28
100 cells, N = 1 square) (**Fig. 1i**). Notably, the distribution of all 1 square responses had a mode at
101 0.25 mV, which is close to previous reports of a 0.2mV somatic response of single synapses in
102 CA1 neurons[23](8845 trials, n = 38 cells, N = 1 square) (**Fig. 1j**).

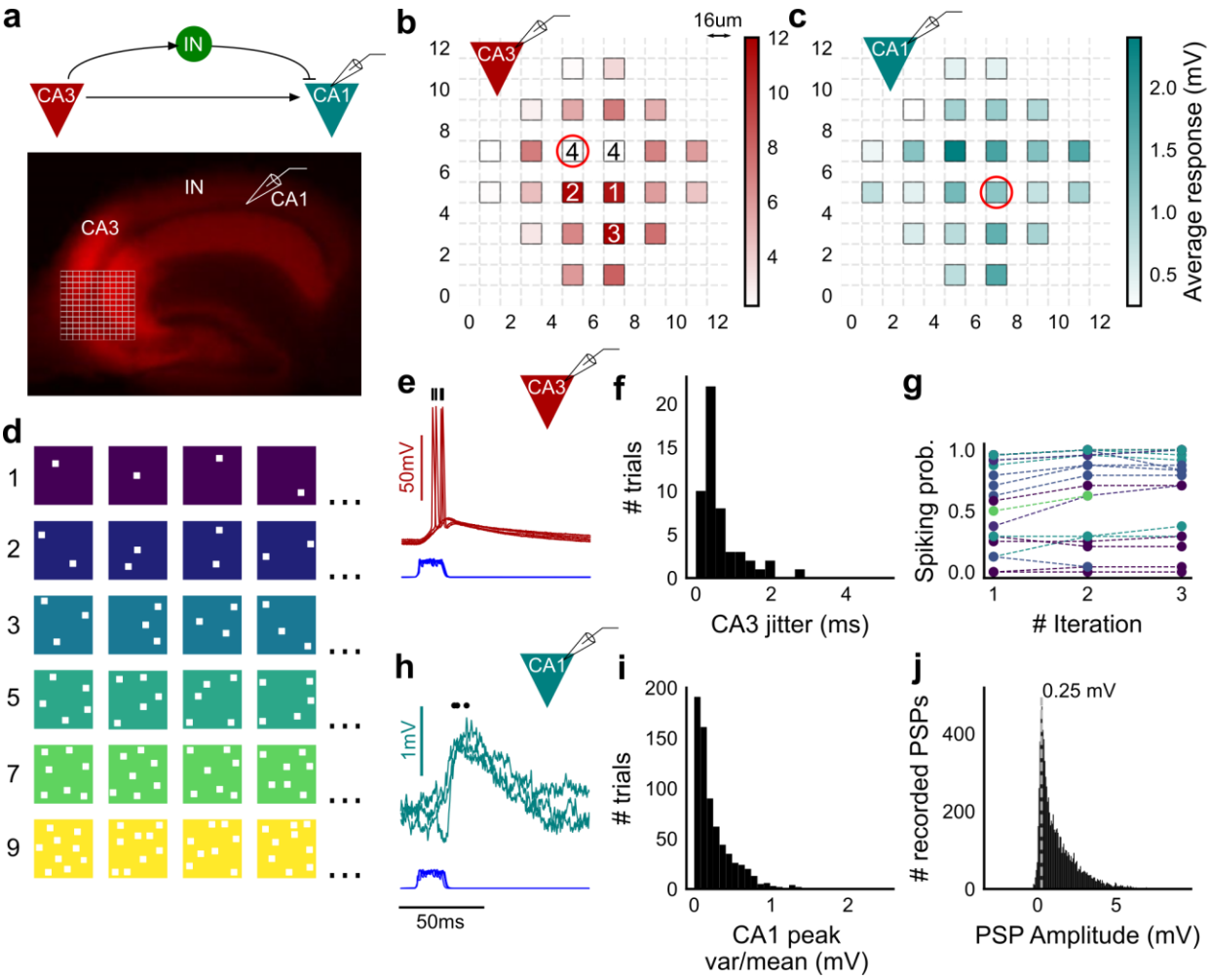

Figure 1: Delivering hundreds of CA3 input combinations to each CA1 neuron using patterned optical stimulation

(**a**) Top, schematic of the CA3-CA1 circuit with direct excitation and feedforward inhibition from CA3 to CA1. Bottom, image of a hippocampus slice expressing ChR2-tdTomato (red) in CA3 in a Cre-dependent manner. In a typical experiment, the optical stimulation grid (not drawn to scale) was centered at the CA3 cell body layer and CA1 neurons were patched.

(**b**) Heat map of CA3 neuron responses with 1 grid square active at a time. A CA3 neuron was patched and optically stimulated, in random temporal order, on the grid locations marked with a gray boundary. There were 24 such 1 square stimuli in the stimulus set. This cell spiked in response to 5 of the squares, marked with numbers inside, which were inferred to be closest to the cell body. Numbers in grid squares

represent the count of trials (out of a total of 4 trials) in which a spike occurred. Color in grid squares represents peak subthreshold membrane potential change from baseline, averaged over trials when a spike did not occur. Locations where the cell spiked all 4 times are in white due to lack of subthreshold depolarizations.

(**c**) Heat map of CA1 responses while CA3 neurons were being stimulated by optical grid with 1 square active at a time. Colormap represents the peak subthreshold membrane potential, averaged over 3 repeats.

(**d**) Schematic of patterned optical stimuli used for stimulating CA3. Examples of input combinations of N-square stimuli (in columns), where N could be 1, 2, 3, 5, 7 or 9 (in rows).

(**e**) Spikes in response to 4 repeats for the square marked with a red circle, in **b**. Spike times are marked with a black tick, showing variability in peak times due to optical stimulation. Blue trace at the bottom marks the stimulus duration, as measured by a photodiode.

(**f**) Distribution of jitter in spike timing (SD) for all squares for all CA3 cells (n=8 cells).

(**g**) Probability of spiking of all CA3 cells tracked over successive repeats within a stimulus epoch of a single recording session. Randomization of the stimulus pattern prevented desensitization of the ChR2 expressing cell. Probability was calculated as the fraction of times a spike happened for a given repeat of all stimuli presented within the epoch. Circles colored as in **d,** depict probability of a spike for one presentation of an N-square stimulus set (n = 7 cells, epochs = 24). Connecting lines track the same input over 3 repeats.

(**h**) PSPs in response to 3 repeats for the square marked with a red circle in **c**. Peak times are marked with an asterisk. Blue trace at the bottom marks the stimulus duration, as measured by a photodiode.

(**i**) Distribution of peak PSP amplitude variability (variance/mean) for all 1-square responses from all cells. (n = 28 cells, stimuli = 695)

(**j**) Histogram of peak amplitudes of all PSPs elicited by all 1-square stimuli, over all CA1 cells (n =38 cells, trials = 8845). Gray dotted line represents the mode of the distribution.

Excitation and inhibition are tightly balanced for all arbitrarily chosen CA3 inputs to a CA1 cell

To examine the relationship between excitation and inhibition, we voltage clamped CA1 neurons, first at the inhibitory (-70 mV) and then at the excitatory (0 mV) reversal potential to record Excitatory and Inhibitory Post Synaptic Currents (EPSCs and IPSCs) respectively. We first presented 5 different patterns of 5 squares each, at both of these potentials, and recorded EPSCs and IPSCs. We found strong proportionality between excitation and inhibition for every stimulus pattern (**Fig. 1d, 2a, b, c**). This suggested that inputs from even random groups of CA3 neurons may be balanced at CA1. Repeats with the same stimulus pattern gave consistent responses, but different patterns evoked different responses (**Fig. 2a**). This indicated that the optically-driven stimuli were able to reliably activate different subsets of synaptic inputs on the target neuron. Next, we asked, in what range of input strengths does random input yield balance? We presented 5 different patterns for each of 1, 2, 3, 5, 7 or 9 square combinations at both recording potentials. Surprisingly, all stimuli to a cell elicited proportional excitatory and inhibitory responses, irrespective of response amplitude (**Fig. 2b, c**) (n = 13 CA1 cells, area under curve, mean R^2 = 0.89+/- 0.06 SD, **Supplementary Figure 2**). Given that the mode of single-square responses was ~0.25 mV, close to single synapse PSP estimates[23] (**Fig. 1j**), we estimate that the granularity of the balance may be of the order of a single synapse. The slope of the regression line through all stimulus-averaged responses for a CA1 cell was used to calculate the Inhibition/Excitation (I/E) ratio for the cell. IPSC/EPSC ratio will be here onwards referred to as I/E ratio, unless explicitly mentioned otherwise. This ratio was typically between 2 and 5 (**Fig. 2f**). The high R^2 values for all cells showed tight proportionality for all stimuli (**Fig. 2g**). The R^2 also remained roughly the same for increasing numbers of spots, again showing that they were not affected by the number of stimulus squares presented (**Fig. 2d,e**). While

166 feedforward inhibition is expected to increase with excitation, convergence of I/E ratios for
167 randomly chosen inputs to a cell to a single number was unexpected. Overall, we found a
168 stimulus-invariant proportionality of excitation and inhibition for any randomly selected input,
169 over a large range of stimulus strengths, suggesting that there is detailed balance[17] in the CA3-
170 CA1 circuit. Since balanced inhibition followed excitation within a few milliseconds(**Fig. 6f,g**), we
171 concluded that the CA3-CA1 feedforward circuit exhibits precise (both detailed and tight)
172 balance[21].

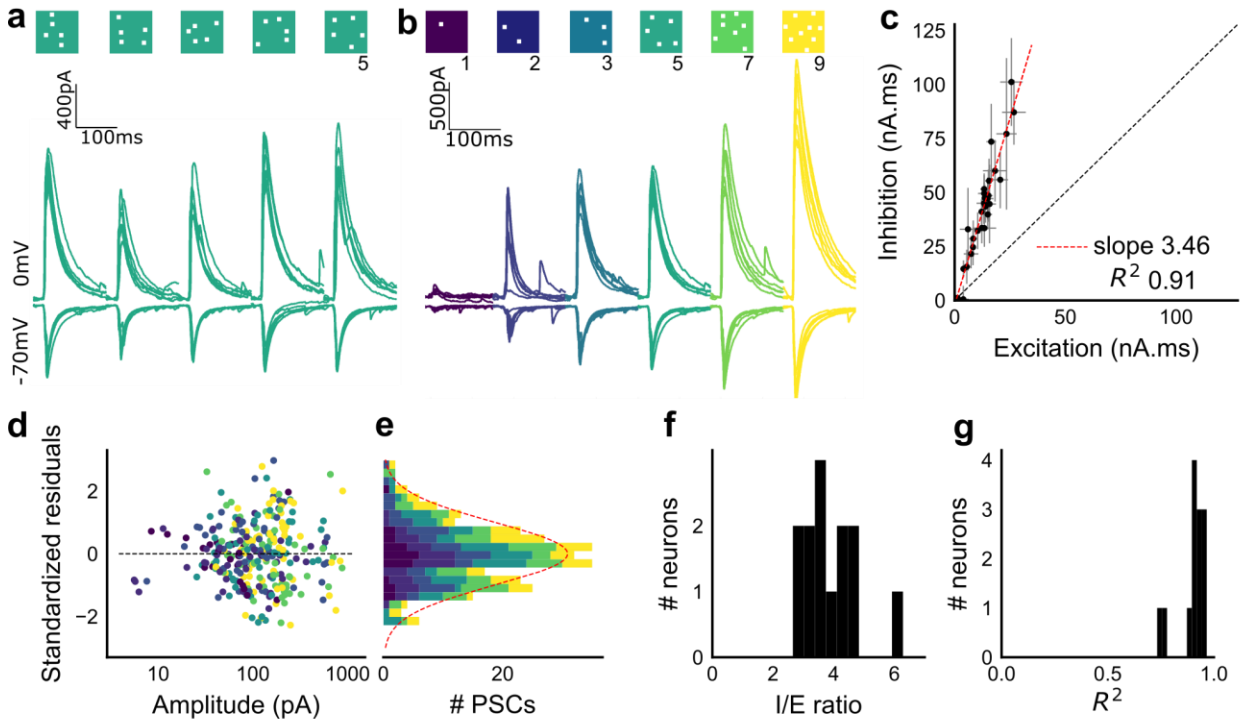

Figure 2: **Excitation and inhibition are tightly balanced for all stimuli to a CA1 cell**

(**a**) Monosynaptic excitatory postsynaptic currents (EPSCs, at -70mV) and disynaptic inhibitory postsynaptic currents (IPSCs, at 0mV) in response to 5 different stimulus combinations of 5 squares each. All combinations show proportional excitatory and inhibitory currents over 6 repeats. Top: schematic of 5 square stimuli.

(**b**) Proportional EPSCs and IPSCs in response to 6 repeats of 1 combination each, from 1 square to 9 square stimulus sets, for the same cell as in a. Top, schematic of the stimuli.

(**c**) Area under the curve for EPSC and IPSC responses, obtained by averaging over 6 repeats, plotted against each other for all stimuli to the cell in **a, b**. Error bars represent SD over repeats.

(**d,e**) Plot of residuals for all inputs (colored by N-square as shown in **b**) of all cells, normalized by their standard deviation, are symmetrically distributed across the regression line at 0. The normalized residuals are normally distributed, as shown in **e**, overlaid with standard normal distribution (red). All responses lie

within two standard deviations, showing absence of outliers. Different N-squares are equally distributed in the different bins in **e**, showing that value of N did not affect the spread of the response.

(**f**) Summary of I/E ratios for all cells (n = 13 cells).

(**g**) Summary for all cells of R^2 values of linear regression fits through all points. Note that 11 out of 13 cells had R^2 greater than 0.9, implying strong proportionality.

Combinatorial CA3 inputs sum sublinearly at CA1

We next asked how CA3 inputs, that lead to balanced excitatory and feedforward inhibitory conductances, transform into membrane potential change at CA1 neurons. Based on anatomical studies, CA3 projections are likely to arrive in a distributed manner over a wide region of the dendritic tree of CA1 pyramidal neuron[24] (**Fig. 3a**). While pairwise summation at CA1 has been shown to be largely linear in absence of inhibition[25], the degree of heterogeneity of summation in response to distributed excitatory and inhibitory synaptic inputs is not well understood (except, see [26]). To avoid biases that may arise from a single response measure during input integration[27], we examined PSPs using four different measures (**Fig. 3c**). These were peak amplitude, area under curve (AUC), average membrane potential and area under curve till peak (**Fig. 3c**).

We looked at input integration by presenting stimulus sets of 5 input squares to a given cell, with each stimulus set ranging from 24 to 225 combinations of inputs. We also recorded the responses to all squares of the grid individually (1 square input). The 1 square PSP response amplitude with inhibition intact (control) was not distinguishable from that with inhibition blocked (GABAzine) (**Methods**, **Supplementary Fig 3**). The 'observed' response for a given square combination was plotted against the 'expected' response, obtained by linearly summing responses of the individual squares constituting that combination (**Fig. 3b, d**). In the absence of inhibition, a multi-square combination of inputs would elicit the same response as the sum of the responses to the individual squares (dotted line, **Fig. 3d**). **Figure 3e** shows responses of a single cell stimulated with 126 distinct 5-square combinations. The 'observed' response was sublinear as compared to the 'expected' summed response, for most stimuli (**Fig. 3e**). For all the four measures in **3c**, CA3 inputs summed sublinearly at CA1 (**Fig. 3e, Supplementary Fig 3**). The sublinear summation suggested that inhibition divisively scales excitation, which was

intuitive, given that excitatory and inhibitory conductances were proportional for all stimuli. For all responses measured over all cells, 93.35% responses were individually sublinear, with distribution having mean 0.57± 0.31 (SD) (**Fig. 3f**). The slope of the regression line, which indicated the extent of sublinearity, varied between cells, with mean 0.38 ± 0.22 (SD) (n = 33 cells) (**Fig. 3g**).

Thus, we found that the CA3-CA1 network exhibits sublinear summation over a large number of inputs.

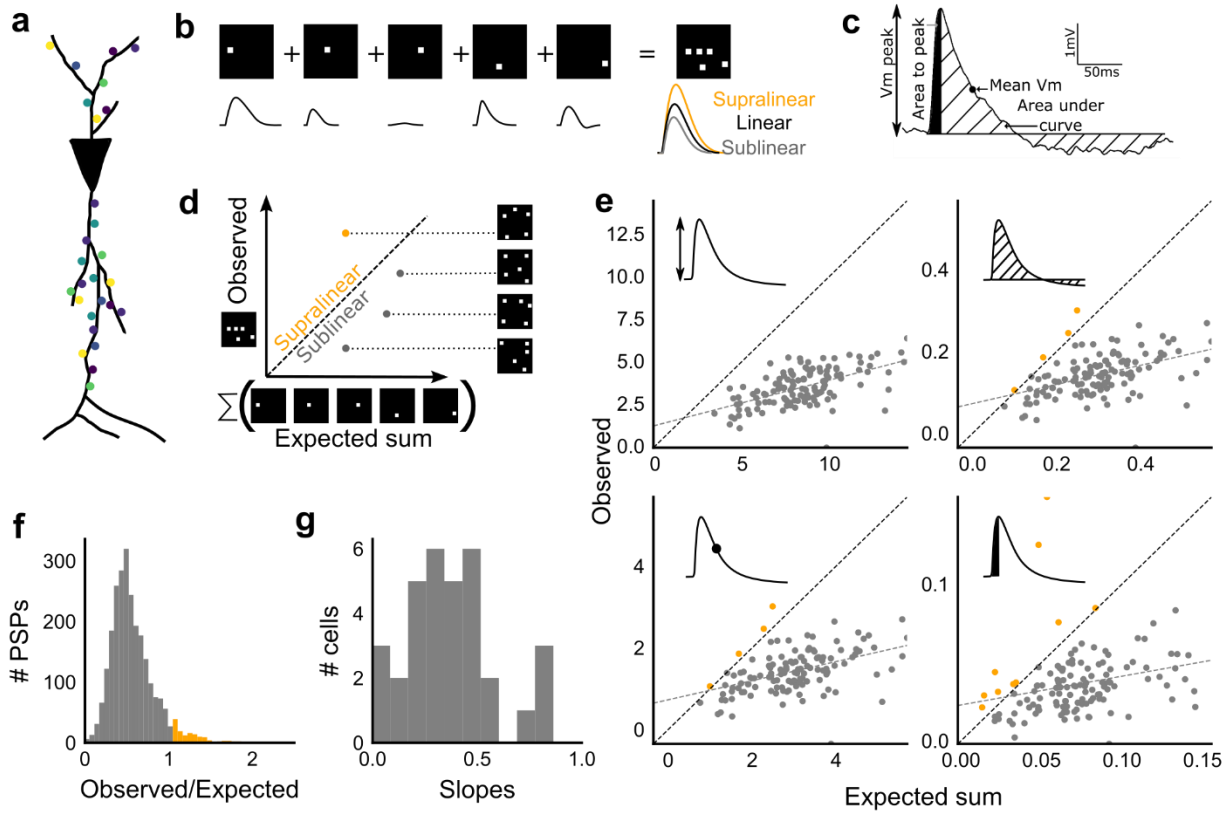

225

226

227 **Figure 3**: **Excitatory and feed-forward inhibitory inputs from CA3 integrate sublinearly at CA1**

228 (**a**) Schematic of a neuron receiving synaptic input distributed over its dendritic tree.

229 (**b**) Schematic of input integration. Top, five 1-square stimuli presented individually, and a single 5-square

230 stimulus comprising of the same squares. Bottom, PSPs elicited as a response to these stimuli. 5-square

231 PSP can be larger (supralinear, orange), equal (linear, black), or smaller (sublinear, gray) than the sum of

232 the single square PSPs.

233 (**c**) A PSP trace marked with the 4 measures used for further calculations. PSP peak, PSP area, area to

234 peak and mean voltage are indicated.

235 (**d**) Schematic of the input integration plot. Each circle represents response to one stimulus combination.

236 'Observed' (true response of 5 square stimulation) on Y-axis and 'Expected' (linear sum of 1 square

237 responses) is on X-axis.

238 (**e**) Most responses for a given cell show sublinear summation for a 5-square stimulus. The 4 panels show

239 sublinear responses for 4 different measures (mentioned in **c**) for the same cell. The grey dotted line is

the regression line and the slope of the line is the scaling factor for the responses for that cell. For peak (mV), area (mV.ms), average (mV), and area to peak (mV.ms); slope = 0.27, 0.23, 0.23, 0.18; R^2 0.57, 0.46, 0.46, 0.26 respectively. The responses to AUC and average are similar because of the similarity in the nature of the measure.

(**f**) Distribution of Observed/Expected ratio of peaks of all responses for all 5-square stimuli (mean= 0.57, SD = 0.31), from all recorded cells pooled. 93.35% responses to 5-square stimuli were sublinear (2513 PSPs, n = 33 cells).

(**g**) Distribution of slopes for peak amplitude of 5-square stimuli (mean = 0.38, SD =0.22). Regression lines for all cells show that all cells display sublinear (<1 slope) summation (n = 33 cells).

CA3-CA1 network performs Subthreshold Divisive Normalization (SDN)

We then tested how summation sublinearity scaled with a larger range of inputs. We noted that nonlinear functions can be observed better with a large range of inputs[27], and therefore increased the stimulus range (**Supplementary Fig 4,5**). Inhibition interacts with excitation to perform arithmetic operations like subtraction, division, and normalization[28]. We created a composite model to fit and test for the above three possibilities of EI integration: subtractive inhibition, divisive inhibition, and divisive normalization (**Eqn. 1**). **Eqn. 1** describes how inhibition controls the 'observed' response (O) as a function of 'expected' response (E), for the above three operations. Alpha (α) can be thought to be a subtractive inhibition parameter, beta (β) as a divisive inhibition parameter, and gamma (γ) a normalization parameter (**Fig. 4a**).

$$O = E - \frac{\beta E}{\gamma + E} E - \alpha \qquad (\mathbf{1})$$

Using the framework of **Eqn. 1**, we asked what computation was performed at the CA3-CA1 network. We recorded from CA1 cells while stimulating CA3 with many combinations of 2,

3, 5, 7 or 9 squares (**Fig. 4b**). We selected cells with at least 50 input combinations, and pooled responses from all stimuli to a cell. Then, we fit equation 1 to the PSP amplitudes (**Fig. 4b**). From visual inspection, the subtractive inhibition model, $O = E - \alpha$ (fixing β, γ=0) was a bad fit, since intercepts (α) were close to 0 (**Fig. 4a**).

By fixing γ and α to 0 in **Eqn. 1,** we obtained the Divisive Inhibition (DI) model. In this form, β can be thought of as inhibition/excitation ratio. Increasing β decreases the observed response (O) (**Fig. 4a**).

$$O = E - \beta E \qquad (\mathbf{2})$$

Similarly, β was fixed to 1 and α to 0 to get the Divisive Normalization (DN) model. This form of the equation was inspired by the analogous canonical divisive normalization equation for firing rates[28]. Here, decrease in γ implies increase in normalization (**Fig. 4a**).

$$O = E - \frac{E}{\gamma + E}E \qquad (\mathbf{3})$$

We used least-squares polynomial regression to fit DI and DN models to our data. The goodness of fit for all cells was tested by comparing BIC (Bayesian Information Criterion) (**Fig. 4c**) and reduced chi-squares of the models (**Supplementary Fig 6, Methods**). DN (α = 0, β = 1) was better than DI (α = 0, γ = 0) model in explaining the data (BIC: Two-tailed paired t-test, $P< 0.00005$, reduced chi-square: Two-tailed paired t-test, $P< 0.00005$, n = 32 cells).

Subthreshold Divisive Normalization (SDN) can be clearly seen in **Figure 4b**, where observed responses to stimuli with 5 mV and 15 mV expected responses are very similar. This shows that SDN allows CA1 cells to integrate a large range of inputs before reaching spike

287 threshold. Thus, testing with a larger range of inputs showed that the initial finding of constant
288 I/E ratios from **Figure 2** needed to be elaborated based on the observed response saturation
289 with increasing input strength. We examine mechanisms for this below (**Figure 5, 6**). In
290 summary, we observed SDN as an outcome of integration of precisely balanced inputs in the
291 CA3-CA1 network.

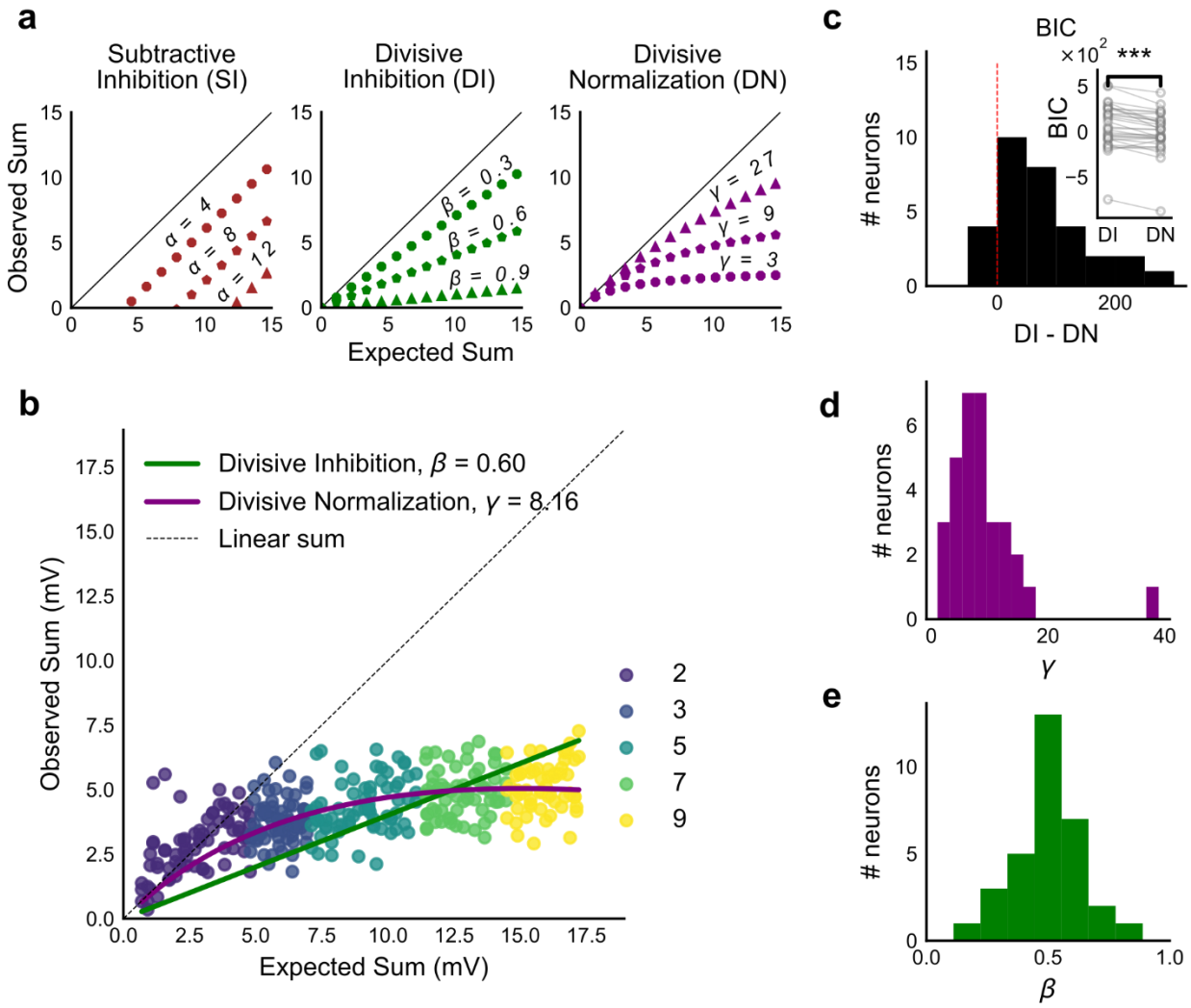

Figure 4: Over a wide input range, integration of CA3 excitatory and feed-forward inhibitory input leads to SDN at CA1

(**a**) Three models of how inhibition interacts with excitation and modulates membrane potential: (left to right) Subtractive Inhibition (SI), Divisive Inhibition (DI) and Divisive Normalization (DN). Note how parameters α, β and γ from Eqn. 1 affect response output.

(**b**) Divisive normalization seen in a cell stimulated with 2, 3, 5, 7 and 9 square combinations. DN and DI model fits are shown in purple and green respectively.

(**c**) Difference in Bayesian Information Criterion (BIC) values for the 2 models - DI and DN. Most differences between BIC for DI and DN were less than 0, which implied that DN model fit better, accounting for the number of variables used. Insets show raw BIC values. Raw BIC values were consistently lower for DN model, indicating better fit (Two-tailed paired t-test, $P< 0.00005$, n = 32 cells). (**d**) Distribution of the parameter γ of the DN fit for all cells (median = 7.9, n = 32 cells). Compare with **a**, **b** to observe the extent of normalization.

(**e**) Distribution of the parameter beta of the DI fit for all cells (mean = 0.5, n = 32 cells). Values are less than 1, indicating sublinear behaviour.

CA3 feedforward inhibition is necessary for subthreshold divisive normalization

We first verified our hypothesis that SDN results from feedforward inhibition from CA3, and not from intrinsic properties of the CA1 neuron. We thus blocked inhibition and repeated the above experiment. We expected that SDN would be lost and linearity would be reinstated upon blocking inhibition.

We recorded responses of CA1 cells to our array of optical stimuli (**Fig. 1d, 5a**), then applied GABAzine to the bath and repeated the stimulus array (**Fig. 5b**). We found that when inhibition was blocked, summation approached linearity (**Fig. 5b, c**). We compared the scaling parameter γ of the divisive normalization model fit, for the above two conditions (**Eqn. 3**). The values of γ were larger with inhibition blocked, indicative of approach to linearity (Wilcoxon rank-sum test, $P<0.05$, n = 8 cells) (**Fig. 5c**). The cells with inhibition blocked showed some residual sublinearity at high stimulus levels, which has been previously attributed to I_A conductance in CA1 neurons[25]. Thus, we confirmed that blocking inhibition reduced sublinearity, attenuating SDN.

Precise balance is also seen at resting membrane potential

Then, we hypothesised that the membrane potential change evoked by inhibitory synaptic currents could be increasing non-linearly with increasing CA3 input. In this scenario, even though the I/E ratio of conductances would be consistent across the range of input strengths, IPSP/EPSP amplitudes would increase nonlinearly. To address this, we compared responses to identical patterns before and after GABAzine application. For a given cell, for each pattern, we subtracted the initial control response with inhibition intact from the corresponding response with inhibition blocked. This gave us the inhibitory component or 'derived inhibition' for each stimulus pattern (**Fig. 5d, inset**). We found that all stimuli to a cell evoked proportional excitation and inhibition even when recorded at resting potential (**Fig. 5d, e**). Thus, we rejected our hypothesis of non-linear increase in inhibitory post-synaptic potential with excitatory post-synaptic potential at resting membrane potential. Over the population, the median slope of the proportionality line was around 0.7, indicating that the EI balance was slightly tilted towards higher excitation than inhibition (**Fig 5f**). IPSP/EPSP ratios (**Fig. 5f**) were smaller than IPSC/EPSC ratios (**Fig. 2f**) due to proximity of inhibition to its reversal (~-70mV), than excitation to its reversal (~0mV), at resting membrane potential (~-65mV). Overall, we saw precise balance in evoked excitatory and inhibitory synaptic potentials for >100 combinations per neuron.

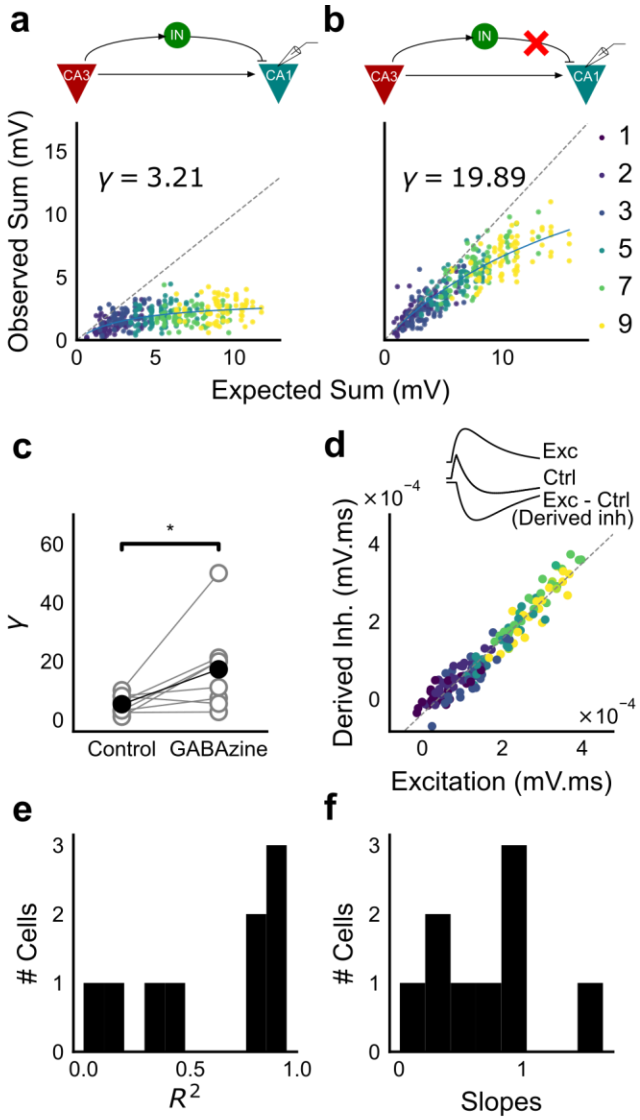

344

345

346 **Figure 5: Blocking balanced inhibition at resting membrane potential attenuates SDN**

347 (**a**) Top, schematic of experiment condition. Bottom, a cell showing divisive normalization in control

348 condition.

349 (**b**) Top, schematic of experiment condition with feedforward inhibition blocked (2uM GABAzine). Bottom,

350 responses of the same cell with inhibition blocked. The responses are much closer to the linear

summation line (dashed). The blue lines in **a**, **b** are the fits of the DN model. The value of γ of the fit increases when inhibition is blocked.

(**c**) The γ of the DN fits were calculated for both control and GABAzine case. Most cells had larger γ with GABAzine in bath (Wilcoxon rank sum test, $P<0.05$, n = 8 cells), implying lower normalization.

(**d**) Excitation versus derived inhibition for all points for the cell shown in **a** (area under the curve) (Slope = 0.97, r-square = 0.93, x-intercept = 3.75e-5 mV.ms). Proportionality was seen for all responses at resting membrane potential. 'Derived inhibition' was calculated by subtracting control PSP from the excitatory (GABAzine) PSP for each stimulus combination.

(**e,f**) R^2 (median = 0.8) and slope values (median = 0.7) for all cells (n = 8 cells), showing tight IPSP/EPSP proportionality, and slightly more excitation than inhibition at resting membrane potentials.

Advancement of inhibitory onset timing with increasing input explains subthreshold divisive normalisation

We made a single compartment conductance model (**Fig. 6a, Eqn. 5**) to analyze the mechanism of SDN. We fit a function of difference of exponentials (**Methods**) to our voltage clamp data to extract the peak amplitudes and kinetics of excitation and inhibition currents (**Methods**). We used these and other parameters from literature (**Supplementary Table 1 and 2**), and constrained the model to have EI balance, i.e. have maximum excitatory (g_{exc}) and inhibitory conductance (g_{inh}) proportional to each other, with a given I/E ratio. To test for SDN, we simulated our model in the range of experimentally determined I/E ratios, ranging from 0-5.

We observed that EI balance with constant EI delay is consistent with the divisive inhibition model (**Fig. 6b**). On the other hand, subthreshold divisive normalization implies progressively smaller changes in peak PSP amplitude with increase in excitatory input. We surmised that without changing EI balance, SDN should result if the inhibitory onset delays were

an inverse function of the excitation (**Fig. 6d**, **Eqn. 4**). Hence, we simulated the model with different values of inhibitory delay (δ_{inh}) as a function of the excitation.

$$\delta_{inh} = \delta_{min} + me^{-kg_{exc}} \quad (4)$$

Here δ_{min} is the minimum synaptic delay between excitation and inhibition, k sets the steepness of the delay change with excitation, and *m* determines the maximum synaptic delay. In **Fig. 6c**, we show that SDN emerged when we incorporated delays changing as a function of the total excitatory input to the model neuron.

We then tested this model prediction. From the EPSC and IPSC fits (**Methods**), we extracted excitatory and inhibitory onsets, and subtracted the average inhibitory onsets from average excitatory onsets to get inhibitory delay (δ_{inh}) for each stimulus combination. We saw that δ_{inh} indeed varied inversely with total excitation (g_{exc}) (**Fig. 6e, f**). Notably, the relationship of delay with conductance with data from all cells pooled, seems to be a single inverse function, and might be a network property (**Fig. 6f, Supplementary Fig 8c**). This input dependent change in inhibitory delay could be attributed to delayed spiking of interneurons with small excitatory inputs, and quicker firing with larger excitatory inputs. Similar relationship between EI latency and strength has been seen in other brain regions[29]. Thus, inhibition clamps down the rising EPSP, resulting in saturation of PSP amplitude when excitation is increased (**Fig. 6c, 8**).

We then examined the sensitivity of SDN to proportionality, and delay between excitation and inhibition. To test if balance and predicted inhibitory delay relationship are required for SDN, we shuffled the balanced g_{inh} in relation with g_{exc}, and separately shuffled the relationship of

398 δ_{inh} and g_{exc}. In both cases, SDN was strongly attenuated, implying that both EI balance and
399 inverse scaling of inhibitory delay were necessary for SDN (**Supplementary Fig 8a, b**).
400
401 Thus our analysis of a conductance model suggests that SDN could be a general
402 property of balanced feedforward networks, due to two characteristic features: EI balance and
403 inhibitory kinetics. Each of these variables may be subject to plasticity and modulation to attain
404 different amounts of normalization (**Fig. 8c,d, Supplementary Fig 9**).

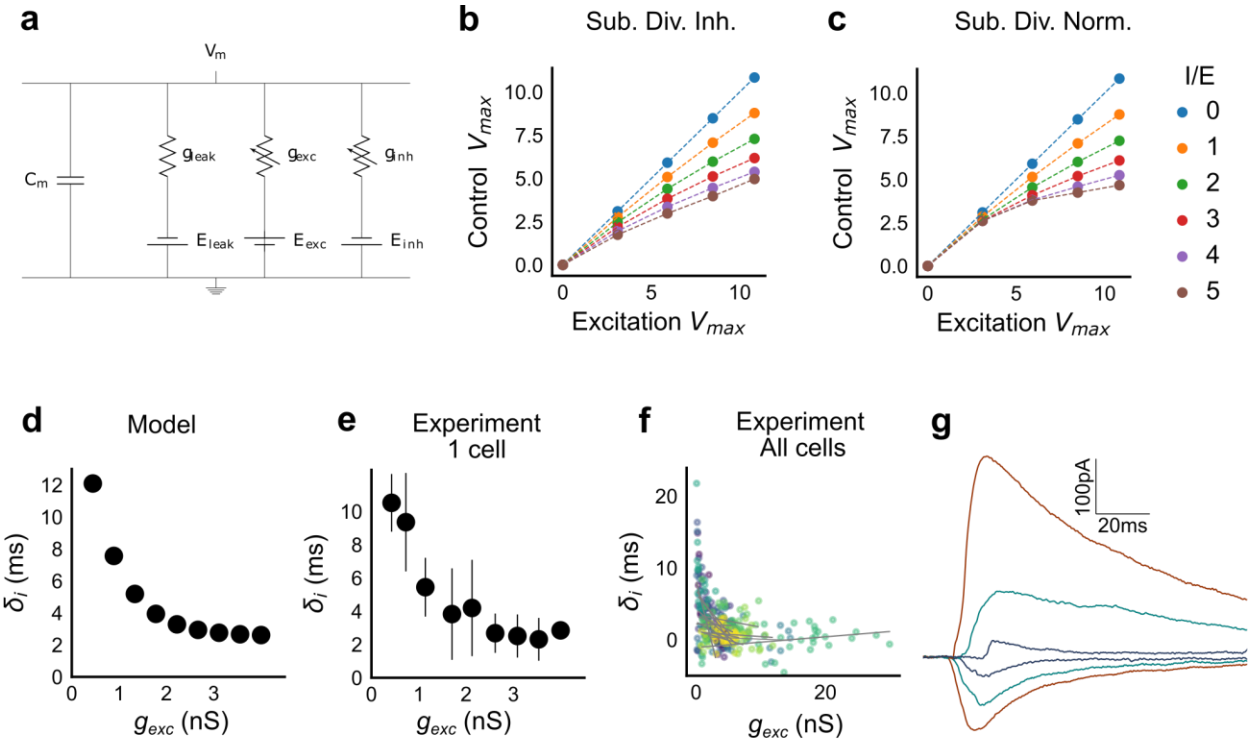

Figure 6: Conductance model predicts Excitatory-Inhibitory delay as an important parameter for divisive normalization.

(**a**) Equivalent circuit for the conductance model showing capacitive, excitatory, inhibitory, and leak components.

(**b**) PSP peak amplitude with both excitatory and balanced inhibitory inputs is plotted against the EPSP peak amplitude with only excitatory input. Model showed divisive inhibition for I/E proportionality ranging from 0 to 5 when the inhibitory delay was kept constant. Different colours show I/E ratios (P).

(**c**) Same as in **b**, except the inhibitory delay was varied inversely with excitatory conductance (as shown in **d)**. Subthreshold Divisive Normalization (SDN) was observed, and the normalization gain was sensitive to the I/E ratio.

(**d**) Inverse relationship of E-I delays with excitation. Inhibitory delay was varied with excitatory conductance in **Eqn. 4** with δ_{min} = 2 ms, k = 2 /nS, and m = 13 ms.

(**e**) Data from an example cell showing the relationship of E-I delays with excitation. The relationship is similar to the prediction in **e**.

(**f**) Data from all cells showing delay as a function of excitation. Different colours indicate different cells (n = 13 cells). Grey lines are linear regression lines through individual cells.

(**g**) Traces showing the decreasing excitatory inhibitory delay with increasing amplitude of PSCs. Each trace is an average of 6 repeats.

Stimulus information is encoded both in amplitude and time

What does SDN mean for information transmission in balanced networks? While SDN allowed the cell to integrate a large range of inputs before reaching spiking threshold, it also resulted in saturation of PSP peaks at larger inputs (**Fig. 4b**). This implied that information about the input was partially 'lost' from the PSP amplitude. However, we observed that due to the decreasing EI delay (δ_{inh}) with increasing excitation (g_{exc}) (**Fig. 6d**), PSP times to peak became shorter, preserving some information about the input in time (**Fig 7a, b, Fig. 8b**). In contrast, while the peak amplitudes seen with GABAzine predicted the input more reliably, peak times of EPSPs did not change much with input (**Fig. 7c,d**). Thus, PSP peak time may carry additional information about stimulus strength, when EI balance is maintained.

We quantified this using an information theoretical framework[30]. We took linear sum of 1 square PSP peak amplitudes (Expected sum), as a proxy for input strength. We then calculated the mutual information between Expected sum and peak PSP amplitudes of the corresponding N-squares, and between Expected sum and PSP peak timing (**Methods**). Using this, we asked, how is the information about the input divided between PSP peak amplitude and timing? We found that peak timing had more information in presence of inhibition (control), and peak amplitude had more information in absence of inhibition (GABAzine) (**Fig. 7f**). The total mutual information of both peak amplitude and peak timing with expected sum was slightly lesser in the

presence of inhibition, but this difference was statistically not significant (**Fig. 7e**) (Wilcoxon Rank sum test (< 0.05), P = 0.4, n = 7 cells). Further, we asked, how better can we predict the input, with the knowledge of peak timing, when the peak amplitude is already known? We found that in the presence of inhibition, peak amplitude carried only a part of the total information about the input, and further knowledge of peak time substantially increased the total information. In contrast, in the absence of inhibition, peak amplitude carried most of the information about input, and there was very little gain in information with the knowledge of peak times (**Fig. 7f**) (Wilcoxon Rank sum test (< 0.05), n = 7 cells).

Overall, these results suggest that with inhibition intact, input information is shared between amplitude and time, and knowledge of peak time and amplitude together contains more information about input than either of them alone.

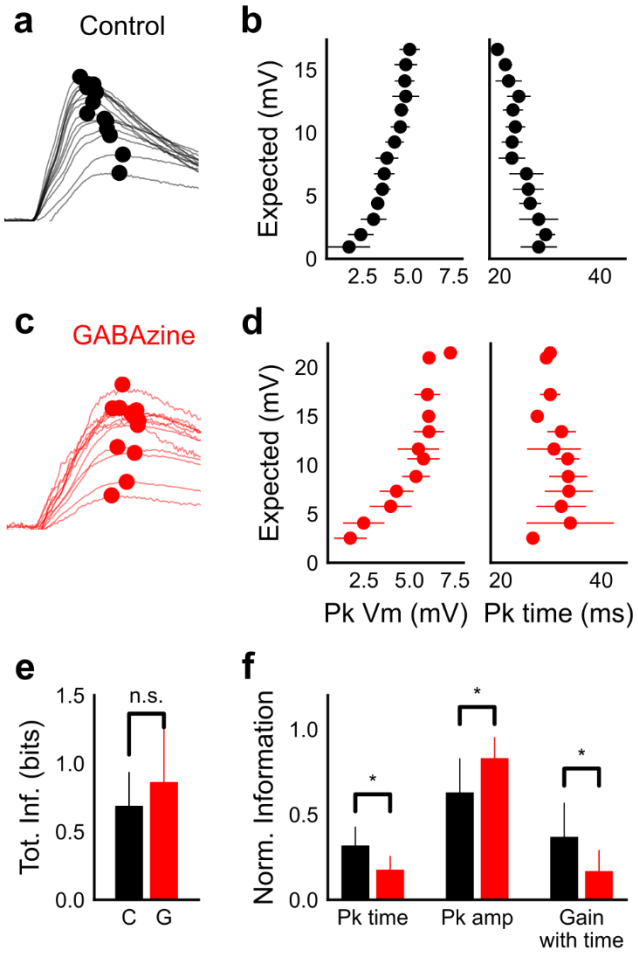

Figure 7: CA3 input strength is encoded in both amplitude and peak time of CA1 PSPs in presence of feedforward inhibition

(**a,c**) The peak arrives earlier as input gets larger in control case (black), but not with GABAzine in bath (red). Averaged traces for an example cell, control (black) and with GABAzine in bath (red). Each trace is averaged over all PSPs within a bin of 'expected sum' strength. Bin centres are as per y axis in panel c.

(**b**) Averaged peak Vm (PSP amplitude) and peak time plotted against Expected Vm. Both amplitude and time change as a function of input (Expected sum).

(**d**) Same as b, but in the presence of GABAzine. As a function of Expected sum, amplitude changes more than control, but time changes less than control.

(**e**) Total mutual information of peak amplitude and peak timing with expected sum is not significantly different between Control and GABAzine case (Wilcoxon Rank sum test (< 0.05), P = 0.4, n = 7 CA1 cells).

(**f**) Normalized mutual information between Expected Vm and peak time, Expected Vm and peak amplitude, and conditional mutual information between Expected Vm and peak time, given the knowledge of peak amplitude. Normalized information was calculated by dividing mutual information by total information (**e**) for each cell. Peak times carry more information in the presence of inhibition, and peak amplitudes carry more information in the absence of inhibition. There is higher gain in information about the input with timing if the inhibition is kept intact (Wilcoxon Rank sum test (P< 0.05), n = 7 CA1 cells).

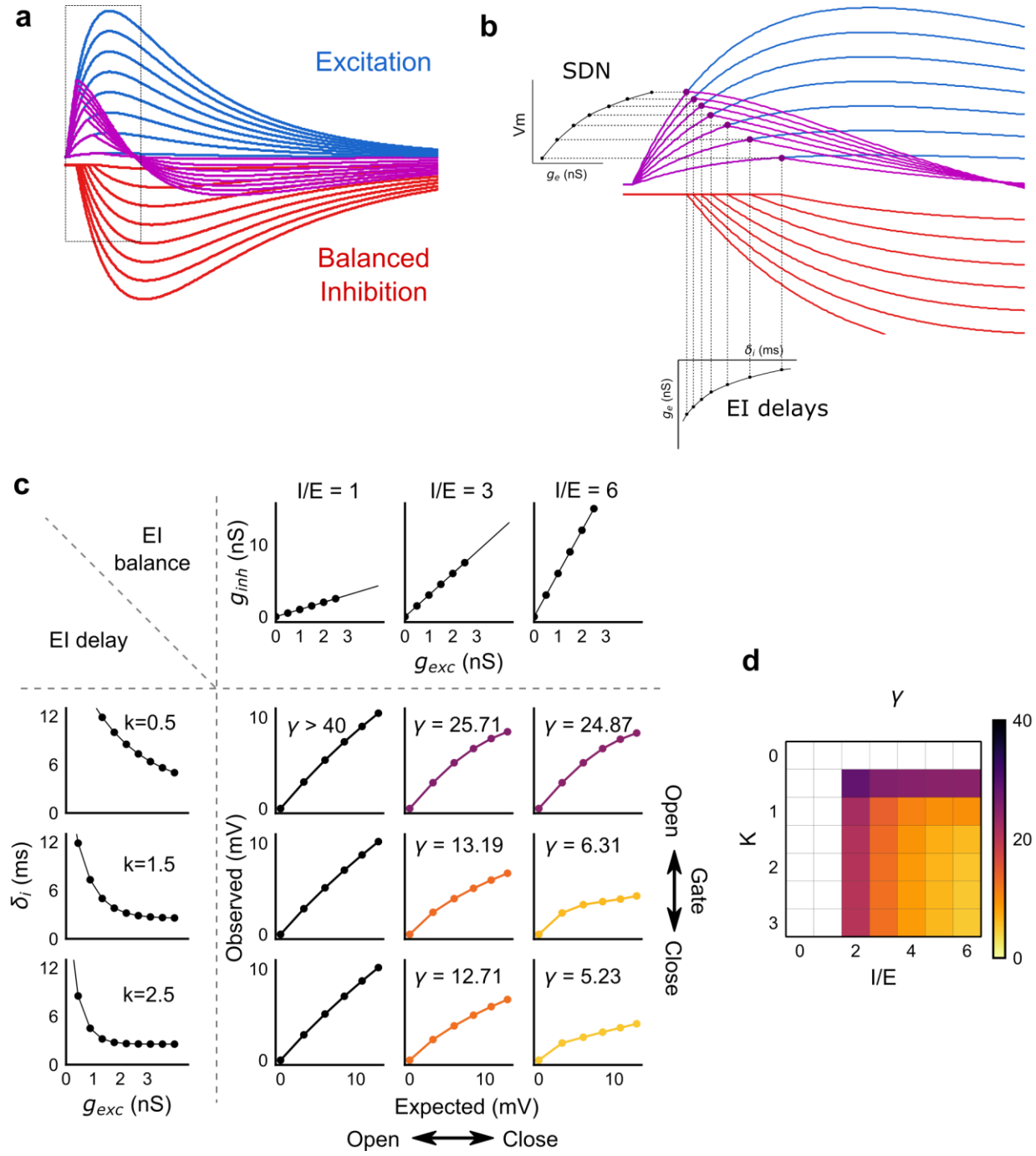

Figure 8: Emergence of SDN from balanced excitation and inhibition, coupled with dynamic EI delays

(**a**) Schematic showing precisely balanced EPSPs (blue) and corresponding IPSPs (red) summing to produce PSPs (purple). The EPSPs and IPSPs increase in equal input steps.

(**b**) Zooming into the portion in the rectangle in **a**. Excitation onset is constant, but inhibition onset changes as an inverse function of input or conductance (g_{exc}), as shown in **Figure 6e**. With increasing input, inhibition arrives earlier and cuts into excitation earlier for each input step. This results in smaller differences in excitatory peaks with each input step, resulting in SDN. The timing of PSP peaks (purple) becomes progressively advanced, whereas the timing of EPSP peaks (blue) does not, consistent with our results in **Figure 7**.

(**c,d**) Normalization as a function of the two building blocks – EI balance (I/E ratio) and EI delays (interneuron recruitment kinetics, k), as predicted by the model. Larger values of both imply greater normalization and increased gating. Colors of the SDN curves depict the value of gamma (γ), as shown in the phase plot in **d**.

DISCUSSION

This study describes two fundamental properties of the CA3-CA1 feedforward circuit: balanced excitation and inhibition from arbitrary presynaptic CA3 subsets, and an inverse relationship of excitatory-inhibitory delays with CA3 input amplitude. By optogenetic photostimulaton of CA3 with hundreds of unique stimulus combinations, we were able to observe precise EI balance at individual CA1 neurons for every input combination presented. Stronger stimuli from CA3 led to proportional increase in excitatory and inhibitory amplitudes at CA1, and a decrease in the delay with which inhibition arrived. Consequently, larger CA3 inputs had shorter inhibitory delays, which led to progressively smaller changes in CA1 membrane potential. We term this gain control mechanism subthreshold divisive normalization (SDN). This

reduction in inhibitory delay with stronger inputs contributes to a division of input strength coding between PSP amplitude and PSP timing.

Precise balance in the hippocampus

We found that arbitrary subsets of synaptic inputs from CA3 to a given CA1 neuron were balanced (**Fig. 2, 5d,e**) and inhibition followed excitation at millisecond timescales (**Fig 6e,f,g**). By targeted optogenetic stimulation of CA3 pyramidal neurons, we eliminated non-specific monosynaptic stimulation of interneurons. This ensured the isolation of the canonical feedforward inhibitory microcircuit in a slice. Our findings demonstrate that precise EI balance is maintained by arbitrary combinations of neurons in the presynaptic network, despite the reduced nature of the slice preparation, with no intrinsic network dynamics. This reveals exceptional structure in the connectivity of the network. Theoretical analyses suggest that networks can achieve detailed balance with inhibitory Spike Timing Dependent Plasticity (iSTDP) rules[21,31,32]. Such an iSTDP rule has been observed in the auditory cortex[33]. Given that balance needs to be actively maintained[34], we suspect that similar plasticity rules[21] may also exist in the hippocampus. Moreover, the change in inhibitory delay with increasing excitatory input may have interesting consequences for any STDP rule such as the inhibitory plasticity rule suggested theoretically[31].

Precisely balanced networks, with all input subsets balanced, are well suited for input gating [21,35]. The finding that most CA1 cells can be converted to place cells predicts the existence of an input gating mechanism [36], but the exact nature of this mechanism has remained unknown. Precise balance at all inputs suggests that although synaptic inputs for several place fields may be sent to a CA1 cell, no place specific activity is observed because all inputs are balanced or gated ‘off’ in default state. Evoked depolarizations[36] or dendritic plateau potentials[37,38], which potentiate the subset of active synapses, ie change I/E ratio[39], can flip the gate ‘on’ for the specific subset of inputs, thereby converting a silent cell to a place cell for that

specific place field. This reasoning corroborates the observation of homogenous inhibition suppressing out-of-field heterogeneously tuned excitation[39], while providing a finer/synaptic scale view of the gating mechanism.

EI delays and temporal coding

In several EI networks in the brain, inhibition is known to suppress excitation after a short time delay, leaving a "window of opportunity" for spiking to occur[2,40,41]. We have shown that balanced inhibitory input arrives with a delay modulated by the excitatory input in a feedforward circuit. This helps encode the input information in both amplitude and timing of the PSP (**Fig. 7**), thus partially decoupling spiking probability from spike timing. In other words, large inputs can be represented with fewer spikes, while conserving input information in spike timing, when naively it would seem that increasing the number of spikes might be the way to represent increasing input. Similar dual encoding has been observed in somatosensory cortex [42]. In CA1, a classic example of dual coding is theta phase precession[43]. In addition, spike times during sharp wave ripples, gamma oscillations and time cell representations are also precise up to ~10ms, which is the range of the dynamic "window of opportunity" we observe. Notably, as the window changes in an excitation dependent manner, the neuron can transition from temporal integration mode at small input amplitudes to coincidence detection at large input amplitudes[2,41,44].

Subthreshold Divisive Normalization (SDN): a novel gain control mechanism

EI balance and dynamic EI delays together give rise to SDN, which modulates synaptic summation gain at single neuron level and determines how much input gets gated to change

556 postsynaptic membrane potential. SDN expands the dynamic range of inputs that a neuron can
557 accommodate before reaching spike threshold (**Supplementary Fig 10**). This is particularly
558 useful for temporally coding, sparse spiking neurons like CA1[45]. Our study was uniquely able to
559 observe SDN because of the large range of inputs possible in our experiments. A narrow range
560 of inputs, similar to what has been used earlier for pairwise summation experiments, is not well
561 suited for characterizing summation nonlinearities, and this limitation has been pointed out by
562 computational analyses[27].
563
564 So far, analogous gain control by divisive normalization has only been observed for firing
565 rates of neurons[28]. Hence, the timescales of gain change in DN are averaged over longer
566 periods, over which rates change. As opposed to this, in SDN, gain of every input is normalized
567 at synaptic (millisecond) timescales. Our results add a layer of subthreshold gain control in
568 single neurons, to the known suprathreshold gain control at the population level in CA1[46] This
569 two-step gain control implies that the dynamic range of the population may be higher than
570 previously estimated.
571
572 Moreover, while most experimental observations of firing rate gain change have been
573 explained by the phenomenological divisive normalization equation, the mechanistic basis for
574 normalization has been unclear. We demonstrate with a clear biophysical model how SDN
575 emerges from interaction of balanced excitatory and inhibitory inputs, connecting our
576 phenomenological model with known biophysics. In our phenomenological SDN model, the
577 parameter γ represents summation gain, or the extent of input gating at CA1 (**Eqn. 1**, **Fig. 4a**). γ
578 is controlled by the following two biophysical quantities: I/E ratio; and the recruitment kinetics of
579 the interneurons (k) (**Eqn. 4, Fig. 8c,d, Supplementary Fig 9**), which can control the amplitude
580 and temporal gate respectively. Dynamic regulation of EI delay has been theoretically explored

in balanced networks[20,47] for temporal gating of inputs, where both amplitude and temporal gates can be independently modulated, and transient inputs can also be gated.

I/E ratio can be changed by neuromodulation[48,49], by short term plasticity mechanisms[50–52] and by disinhibition[53]. Although we show that EI delays are input amplitude dependent, they may be modulated by external signals, or behavioural states, such as attention[54] to gate the output of individual neurons (**Fig. 8c,d**). For example, interneuron recruitment based changes have been shown to exist in thalamocortical neurons[44] . Thus, temporal gating by EI delays[20], combined with the amplitude gating by detailed balance[17] could be a powerful mechanism for gating signals[20] in the hippocampal feedforward microcircuit.

Several studies point towards the existence of precise EI balance in the cortex[2–4,11–13], and here we have shown it in the hippocampus. We propose that input strength dependent inhibitory delay change may be a general property of feedforward network motifs. Together, these suggest that precisely balanced feedforward networks are elegantly suited for controlling gain, timing and gating at individual neurons in neural circuits.

METHODS

Animals

All experimental procedures were approved by the National Centre for Biological Sciences Institutional Animal Ethics Committee (Protocol number USB–19–1/2011), in accordance with the guidelines of the Government of India (animal facility CPCSEA registration number 109/1999/CPCSEA) and equivalent guidelines of the Society for Neuroscience. CA3-cre (C57BL/6-Tg (Grik4-cre) G32-4Stl/J mice, Stock number 006474) were obtained from Jackson Laboratories. The animals were housed in a temperature controlled environment with a 14-h light: 10h dark cycle, with *ad libitum* food and water.

Virus injections

21-30 days old male transgenic mice were injected with Lox-ChR2 (AAV5.CAGGS.Flex.ChR2-tdTomato.WPRE.SV40) virus obtained from University of Pennsylvania Vector Core. Injection coordinates used were -2.0mm RC, +/-1.9mm ML, -1.5mm DV. ~300-400nl solution was injected into the CA3 region with brief pressure pulses using Picospritzer-III (Parker-Hannifin, Cleveland, OH, USA). Animals were allowed to recover for at least 4 weeks following surgery.

Slice Preparation

8-6 week (4-8 weeks post virus injection) old mice were anesthetized with halothane and decapitated post cervical dislocation. Hippocampus was dissected out and 350um thick transverse hippocampal slices were prepared. Slices (350 microns) were cut in ice-cold high sucrose ASCF containing (in mM) - 87 NaCl, 2.5 KCl, 1.25 NaH2PO4, 25 NaHCO3, 75 sucrose, 10 glucose, 0.5 CaCl2, 7 MgCl2. For cut slice control experiments, CA3 was removed at this stage. Slices were stored in a holding chamber, in artificial cerebro-spinal fluid (aCSF)

containing (in mM) - 124 NaCl, 2.7 KCl, 2 CaCl2, 1.3 MgCl2, 0.4 NaH2PO4, 26 NaHCO3, and 10 glucose, saturated with 95% O2/5% CO2. After at least an hour of incubation, the slices were transferred to a recording chamber and perfused with aCSF at room temperature.

Electrophysiology

Whole cell recording pipettes of 2-5MO were pulled from thick-walled borosilicate glass on a P-97 Flaming/Brown micropipette puller (Sutter Instrument, Novato, CA). Pipettes were filled with internal solution containing (in mM) 130 K-gluconate, 5 NaCl, 10 HEPES, 1 EGTA, 2 MgCl2, 2 Mg-ATP, 0.5 Na-GTP and 10 Phosphocreatinine, pH adjusted to 7.3, osmolarity ~285mOsm. The membrane potential of CA1 cells was maintained near -65mV, with current injection, if necessary. GABA-A currents were blocked with GABAzine (SR-95531, Sigma) at 2uM concentration for some experiments. Cells were excluded from analysis if the input resistance changed by more than 25% (measured for 15/39 cells) or if membrane voltage changed more than 2.5mV (measured for 39/39 cells, maximum current injected to hold the cell at the same voltage was +/-15 pA) of the initial value. For voltage clamp recordings, the K-gluconate was replaced by equal concentration Cs-gluconate. Cells were voltage clamped at 0mV (close to calculated excitation reversal) and -70mV (calculated inhibition reversal) for IPSC and EPSC recordings respectively. At 0mV a small component of APV sensitive inward current was observed, and was not blocked during recordings. Cells were excluded if series resistance went above 25MO or if it changed more than 30% of the initial value, with mean series resistance being 15.7MO +/- 4.5MO std (n=13). For CA3 current clamp recordings, the cells were excluded if the Vm changed by 5mV of the initial value. For whole-cell recordings, neurons were visualized using infrared microscopy and differential interference contrast (DIC) optics on

an upright Olympus BX61WI microscope (Olympus, Japan) fitted with a 40X (Olympus LUMPLFLN, 40XW), 0.8NA water immersion objective.

Data Acquisition

Recordings were acquired on a HEKA EPC10 double plus amplifier (HEKA Electronik, Germany) and filtered 2.9 kHz and digitized at 20 kHz. All analysis was done using custom written software in Python 2.7.12 and Matlab R2012b.

Optical stimulation setup

Optical stimulation was done using DMD (Digital Micromirror Device) based Optoma W316 projector (60Hz refresh rate) with its color wheel removed. Image from the projector was miniaturized using a Nikon 50mm f/1.4D lens and formed at the focal plane of the tube lens, confocal to the sample plane. The white light from the projector was filtered using a blue filter (Edmund Optics, 52532), reflected off of a dichroic mirror (Q495LP, Chroma), integrated into the light path of the Olympus microscope, and focused on sample through a 40X objective. This arrangement covered a circular field of around 200 micron diameter on sample. 2.5 pixels measured 1 micron at sample through the 40X objective. Light intensity, measured using a power meter, was about 150mW/mm^2 at sample surface. Background light from black screen usually elicited no or very little synaptic response at recorded CA1 cells. A shutter (NS15B, Uniblitz) was present in the optical path to prevent the slice from being stimulated by background light during the inter-trial interval. The shutter was used to deliver stimulus of 10-

15ms per trial. A photodiode was placed in the optical path after the shutter to record timestamps of the delivered stimuli.

Patterned optical stimulation

Processing 2 was used for generating optical patterns. All stimuli were 16 micron squares sub sampled from a grid. 16 micron was chosen since it is close to the size of a CA3 soma. The light intensity and square size were standardized to elicit typically 1 spike per cell per stimulus. The number of spikes varied to some extent based on the expression of ChR2, which varied from cell to cell. The switching of spots from one trial to next, at 3 sec inter trial interval, prevented desensitization of ChR2 over successive trials (**Fig. 1g**).

For a patched CA1 cell, the number of connected CA3 neurons stimulated per spot was estimated to be in the range of 1 to a maximum of 50 for responses ranging from 0 to 2mV. These calculations were done assuming a contribution of 0.2mV per synapse[23] and release probability of ~0.2[55]. This number includes responses from passing axons, which could also get stimulated in our preparation.

We did not observe any significant cross stimulation of CA1 cells. CA1 cells were patched and the objective was shifted to the CA3 region of the slice, where the optical patterns were then projected. CA1s showed no response to optical stimulation because of (i) ChR2 was restricted to CA3 cells, (ii) physical shifting of the objective away from CA1 also made sure that any leaky expression, if present, did not elicit responses.

We used 4 different stimulus grids (**Supplementary Fig 11**). All squares from a grid were presented individually (in random order) and in a stimulus set - randomly chosen

combinations of 2, 3, 5, 7, or 9, with 2 or 3 repeats of each combination. The order of presentation of a given N square combination was randomized from cell to cell.

Data Analysis

Data analysis was done using Python, numpy, scipy, matplotlib and other free libraries. All analysis code is available as a free library at (https://github.com/sahilm89/linearity).

Pre-processing

PSPs and PSCs were filtered using a low pass Bessel filter at 2 kHz, and baseline normalized using 100 ms before the optical stimulation time as the baseline period. Period of interest was marked as 100 ms from the beginning of optical stimulation, as it was the typical timescales of PSPs. Timing of optical stimulation was determined using timestamp from a photodiode responding to the light from the projector. Trials were flagged if the PSP in the interest period were indistinguishable from baseline period due to high noise, using a 2 sample KS test (p-value < 0.05). Similarly, action potentials in the interest period were flagged and not analyzed, unless specifically mentioned.

Feature extraction

A total of 4 measures were used for analyzing PSPs and PSCs (**Fig. 3c**). These were mean, area under the curve, average and area to peak. This was done to be able to catch differences in integration at different timescales, as suggested by Poirazi et al[27]. Trials from CA1 were mapped back to the grid locations of CA3 stimulation for comparison of Expected and

Observed responses. Grid coordinate-wise features were calculated by averaging all trials for a given grid coordinate.

Subthreshold Divisive Normalization model

Different models of synaptic integration: Subtractive Inhibition, Divisive Inhibition, and Divisive Normalization models were obtained by constraining parameters in **Equation 1**. The models were then fit to the current clamp dataset using lmfit. Reduced chi-squares

(**Supplementary Fig 6**) and Bayesian Information Criterion (**Fig 4c**) were used to evaluate the goodness of fits of these models to experimental data.

Single compartment model

A single compartment conductance based model was created in Python using sympy and numpy. The model consisted of leak, excitatory and inhibitory synaptic conductances (**Eqn.5**, **Fig 6a**) to model the subthreshold responses by the CA1 neurons.

$$C_m \frac{dV_m}{dt} = g_{leak}(V_m - E_{leak}) + g_{exc}(V_m - E_{exc}) + g_{inh}(V_m - E_{inh}) \quad (5)$$

The parameters used for the model were taken directly from data, or literature (Supplementary **Table 2**). The synaptic conductances $g_{exc}(t)$, and $g_{inh}(t)$ were modeled as difference of exponentials (**Eqn. 6 and 7**):

$$g_{exc}(t) = \bar{g}_{exc} \left(\frac{e^{\left(\frac{-t}{\tau_{decay}}\right)} - e^{\left(\frac{-t}{\tau_{rise}}\right)}}{-\left(\frac{\tau_{rise}}{\tau_{decay}}\right)^{\frac{\tau_{decay}}{\tau_{decay}-\tau_{rise}}} + \left(\frac{\tau_{rise}}{\tau_{decay}}\right)^{\frac{\tau_{rise}}{\tau_{decay}-\tau_{rise}}}} \right) \quad (6)$$

$$g_{inh}(t) = \bar{g}_{inh} \left(\frac{e^{\left(\frac{\delta_{inh}-t}{\tau_{decay}}\right)} - e^{\left(\frac{\delta_{inh}-t}{\tau_{rise}}\right)}}{-\left(\frac{\tau_{rise}}{\tau_{decay}}\right)^{\frac{\tau_{decay}}{\tau_{decay}-\tau_{rise}}} + \left(\frac{\tau_{rise}}{\tau_{decay}}\right)^{\frac{\tau_{rise}}{\tau_{decay}-\tau_{rise}}}} \right) \quad (7)$$

730 For the divisive normalization case, the inhibitory delays (δ_{inh}) were modelled to be an
731 inverse function of $g_{exc}(t)$ (**Eqn.4**). In other cases, they were assumed to be constant and
732 values were taken from **Supplementary Table 2**.

733

734 ## Fitting data

735 Voltage clamp data was fit to a difference of exponential functions (**Eqn.8,**
736 **Supplementary Fig 7**) by a non-linear least squares minimization algorithm using lmfit, a freely
737 available curve fitting library for Python. Using this, we obtained amplitudes ($\overline{g}$), time course
738 (τ_{rise},τ_{decay}) and onset delay from stimulus (δ_{onset}) for both excitatory and inhibitory currents.
739 We then calculated inhibitory onset delay (δ_{inh}) by subtracting onset delayof excitatory from
740 inhibitory traces.

741

$$g(t) = \overline{g}\left(\frac{e^{\left(\frac{\delta_{onset} - t}{\tau_{decay}}\right)} - e^{\left(\frac{\delta_{onset} - t}{\tau_{rise}}\right)}}{-\left(\frac{\tau_{rise}}{\tau_{decay}}\right)^{\frac{\tau_{decay}}{\tau_{decay} - \tau_{rise}}} + \left(\frac{\tau_{rise}}{\tau_{decay}}\right)^{\frac{\tau_{rise}}{\tau_{decay} - \tau_{rise}}}}\right) \quad \textbf{(8)}$$

742 ## Onset detection

743 Onsets were also detected using 3 methods. Since we propose onset delays to be a
744 function of the excitation peak, we avoided onset finding methods such as time to 10% of peak,
745 which rely on peaks of the PSCs. We used threshold based (time at which the PSC crossed a
746 threshold), slope based (time at which the slope of the PSC onset was the steepest) and a
747 running window based methods. In the running window method, we run a short window of 0.5
748 ms, and found the time point at which distributions of two consecutive windows became

749 dissimilar, using a 2 sample KS test. Ideally, with no input, the noise distribution across two
750 consecutive windows should remain identical. All 3 methods gave qualitatively similar results.

751 **Mutual Information calculation**

752 Mutual information was calculated by the histogram method. The calculated linear sum
753 from one square PSP peak amplitude responses, measured N-square peak amplitudes and
754 time were binned with equal number of bins. The bins were calculated using Sturges' Rule. Bin
755 frequencies were divided by the total number of responses to get the probability of

occurrence$p(x)$ of each bin. Mutual Information was then calculated for all pairs of combinations between linear sum, peak amplitude and time using **Eqn.9 and 10**.

$$MI(X,Y) = H(X) + H(Y) - H(X,Y) \quad (9)$$

Where Shannon's entropy$H(X)$ for a variable X, is given as:

$$H(X) = \sum_{x \in X} - p(x) \log_2 p(x) \quad (10)$$

Further, conditional mutual Information was calculated to measure gain in information about input (linear sum) by knowledge of peak timing when peak amplitude is already known. It was calculated using **Equation 11**.

$$I(X;Y|Z) = H(X,Z) + H(Y,Z) - H(X,Y,Z) - H(Z) \quad (11)$$

Normalized mutual information was calculated by dividing mutual information between pairs of variables by the total information between all three variables (**Equation 12**).

$$I(X;Y,Z) = H(Z) + H(X,Y) - H(X,Y,Z) \quad (12)$$

ACKNOWLEDGEMENTS

AB and SM were supported by NCBS/TIFR and Council of Scientific and Industrial Research (CSIR). We acknowledge support from the University Grants Commission/Israel Science Foundation grant (UGC/ISF No. F 6-18/2014(IC)). We acknowledge the National Mouse Resource (NaMoR) facility funded by Department of Biotechnology for housing and maintaining all animals used in this study. We would like to thank Nikhila Krishnan and Shriya Palchaudhuri for help with genotyping; and Kambadur Ananthamurthy, Sathyaa Subramaniyam, Deepanjanli Dwivedi, Oliver Muthmann, Mehrab Modi, Dinesh Natesan, Aditya Gilra, Arvind Kumar and Rishikesh Narayanan for discussions and suggestions on the manuscript.

AUTHOR CONTRIBUTIONS

AB, SM and USB designed the study. AB performed the experiments and did part of the analysis. SM did most of the analysis and implemented the models. All authors wrote the manuscript.

REFERENCES

1. Anderson, J. S., Carandini, M. & Ferster, D. Orientation tuning of input conductance, excitation, and inhibition in cat primary visual cortex. *J. Neurophysiol.* **84,** 909–926 (2000).
2. Wehr, M. & Zador, A. M. Balanced inhibition underlies tuning and sharpens spike timing in auditory cortex. *Nature* **426,** 442–446 (2003).
3. Okun, M. & Lampl, I. Instantaneous correlation of excitation and inhibition during ongoing and sensory-evoked activities. *Nat. Neurosci.* **11,** 535–7 (2008).
4. Atallah, B. V & Scanziani, M. Instantaneous Modulation of Gamma Oscillation Frequency

by Balancing Excitation with Inhibition. *Neuron* **62,** 566–577 (2009).

5. Okun, M. & Lampl, I. Balance of excitation and inhibition. *Scholarpedia* **4,** 7467 (2009).

6. Yizhar, O. *et al.* Neocortical excitation/inhibition balance in information processing and social dysfunction. *Nature* **477,** 171–178 (2011).

7. Isaacson, J. S. & Scanziani, M. How inhibition shapes cortical activity. *Neuron* **72,** 231–243 (2011).

8. Silver, R. A. Neuronal arithmetic. **11,** (2010).

9. Chance, F. S., Abbott, L. F. & Reyes, A. D. Gain modulation from background synaptic input. *Neuron* **35,** 773–782 (2002).

10. Reynolds, J. H. & Heeger, D. J. The Normalization Model of Attention. *Neuron* **61,** 168–185 (2009).

11. Zhang, L. I., Tan, A. Y. Y., Schreiner, C. E. & Merzenich, M. M. Topography and synaptic shaping of direction selectivity in primary auditory cortex. *Nature* **424,** 201–205 (2003).

12. Zhou, M. *et al.* Scaling down of balanced excitation and inhibition by active behavioral states in auditory cortex. *Nat. Neurosci.* **17,** 841–850 (2014).

13. Wilent, W. B. & Contreras, D. Dynamics of excitation and inhibition underlying stimulus selectivity in rat somatosensory cortex. *Nat. Neurosci.* **8,** 1364–1370 (2005).

14. Shu, Y., Hasenstaub, A., Badoual, M., Bal, T. & McCormick, D. A. Barrages of Synaptic Activity Control the Gain and Sensitivity of Cortical Neurons. *J. Neurosci.* **23,** (2003).

15. Haider, B., Duque, A., Hasenstaub, A. R. & McCormick, D. A. Neocortical Network Activity In Vivo Is Generated through a Dynamic Balance of Excitation and Inhibition. *J. Neurosci.* **26,** (2006).

16. Denève, S. & Machens, C. K. Efficient codes and balanced networks. *Nat. Neurosci.* **19,** 375–82 (2016).

17. Vogels, T. P. & Abbott, L. F. Gating multiple signals through detailed balance of excitation

and inhibition in spiking networks. *Nat. Neurosci.* **12,** 483–91 (2009).

18. van Vreeswijk, C. & Sompolinsky, H. Chaos in neuronal networks with balanced excitatory and inhibitory activity. *Science* **274,** 1724–6 (1996).

19. Shadlen, M. N. & Newsome, W. T. The variable discharge of cortical neurons: implications for connectivity, computation, and information coding. *J. Neurosci.* **18,** 3870–96 (1998).

20. Kremkow, J., Aertsen, A. & Kumar, A. Gating of Signal Propagation in Spiking Neural Networks by Balanced and Correlated Excitation and Inhibition. *J. Neurosci.* **30,** 15760–15768 (2010).

21. Hennequin, G., Agnes, E. J. & Vogels, T. P. Inhibitory Plasticity: Balance, Control, and Codependence. *Annu. Rev. Neurosci.* **40,** annurev-neuro-072116-031005 (2017).

22. Ishizuka, N., Cowan, W. M. & Amaral, D. G. A quantitative analysis of the dendritic organization of pyramidal cells in the rat hippocampus. *J Comp Neurol* **362,** 17–45 (1995).

23. Magee, J. C. & Cook, E. P. Somatic EPSP amplitude is independent of synapse location in hippocampal pyramidal neurons. *Nat. Neurosci.* **3,** 895–903 (2000).

24. Ishizuka, N., Weber, J. & Amaral, D. G. Organization of intrahippocampal projections originating from CA3 pyramidal cells in the rat. *J. Comp. Neurol.* **295,** 580–623 (1990).

25. Cash, S. & Yuste, R. Linear summation of excitatory inputs by CA1 pyramidal neurons. *Neuron* **22,** 383–394 (1999).

26. Lovett-Barron, M. *et al.* Regulation of neuronal input transformations by tunable dendritic inhibition. *Nat. Neurosci.* **15,** 423–30, S1-3 (2012).

27. Poirazi, P., Brannon, T. & Mel, B. W. Arithmetic of Subthreshold Synaptic Summation in a Model CA1 Pyramidal Cell. *Neuron* **37,** 977–987 (2003).

28. Carandini, M. & Heeger, D. Normalization as a canonical neural computation. *Nat. Rev.*

Neurosci. 1–12 (2012). doi:10.1038/nrn3136

29. Heiss, J. E., Katz, Y., Ganmor, E. & Lampl, I. Shift in the Balance between Excitation and Inhibition during Sensory Adaptation of S1 Neurons. *J. Neurosci.* **28,** 13320–13330 (2008).

30. Shannon, C. E. A Mathematical Theory of Communication. *Bell Syst. Tech. J.* **27,** 379–423 (1948).

31. Vogels, T. P., Sprekeler, H., Zenke, F., Clopath, C. & Gerstner, W. Inhibitory plasticity balances excitation and inhibition in sensory pathways and memory networks. *Science* **334,** 1569–73 (2011).

32. Luz, Y. & Shamir, M. Balancing feed-forward excitation and inhibition via hebbian inhibitory synaptic plasticity. *PLoS Comput. Biol.* **8,** (2012).

33. D'amour, J. A. & Froemke, R. C. Inhibitory and Excitatory Spike-Timing-Dependent Plasticity in the Auditory Cortex. *Neuron* **86,** 514–528 (2015).

34. Xue, M., Atallah, B. V. & Scanziani, M. Equalizing excitation–inhibition ratios across visual cortical neurons. *Nature* **511,** 596–600 (2014).

35. Barron, H. C., Vogels, T. P., Behrens, T. E. & Ramaswami, M. Inhibitory engrams in perception and memory. *Proc. Natl. Acad. Sci.* **114,** 201701812 (2017).

36. Lee, D., Lin, B.-J. & Lee, A. K. Hippocampal Place Fields Emerge upon Single-Cell Manipulation of Excitability During Behavior. *Science (80-.).* **337,** 849–853 (2012).

37. Bittner, K. C. *et al.* Conjunctive input processing drives feature selectivity in hippocampal CA1 neurons. *Nat. Neurosci.* **18,** 1133–1142 (2015).

38. Bittner, K. C., Milstein, A. D., Grienberger, C., Romani, S. & Magee, J. C. Behavioral time scale synaptic plasticity underlies CA1 place fields. *Science (80-.).* **357,** 1033–1036 (2017).

39. Grienberger, C., Milstein, A. D., Bittner, K. C., Romani, S. & Magee, J. C. Inhibitory suppression of heterogeneously tuned excitation enhances spatial coding in CA1 place

cells. *Nat. Neurosci.* **20,** 417–426 (2017).

40. Pouille, F. & Scanziani, M. Enforcement of temporal fidelity in pyramidal cells by feed-forward somatic inhibition. *Science (80-.).* **293,** 325–331 (2001).

41. Higley, M. J. & Contreras, D. Balanced Excitation and Inhibition Determine Spike Timing during Frequency Adaptation. *J. Neurosci.* **26,** 448–457 (2006).

42. Panzeri, S., Petersen, R. S., Schultz, S. R., Lebedev, M. & Diamond, M. E. The role of spike timing in the coding of stimulus location in rat somatosensory cortex. *Neuron* **29,** 769–777 (2001).

43. Jensen, O. & Lisman, J. E. Position Reconstruction From an Ensemble of Hippocampal Place Cells: Contribution of Theta Phase Coding. *J. Neurophysiol.* **83,** 2602–2609 (2000).

44. Gabernet, L., Jadhav, S. P., Feldman, D. E., Carandini, M. & Scanziani, M. Somatosensory integration controlled by dynamic thalamocortical feed-forward inhibition. *Neuron* **48,** 315–327 (2005).

45. Ahmed, O. J. & Mehta, M. R. The hippocampal rate code: anatomy, physiology and theory. *Trends in Neurosciences* **32,** 329–338 (2009).

46. Pouille, F., Marin-Burgin, A., Adesnik, H., Atallah, B. V. & Scanziani, M. Input normalization by global feedforward inhibition expands cortical dynamic range. *Nat. Neurosci.* **12,** 1577–85 (2009).

47. Bruno, R. M. Synchrony in sensation. *Current Opinion in Neurobiology* **21,** 701–708 (2011).

48. Froemke, R. C. Plasticity of Cortical Excitatory-Inhibitory Balance. *Annu. Rev. Neurosci.* **38,** 195–219 (2015).

49. Froemke, R. C., Merzenich, M. M. & Schreiner, C. E. A synaptic memory trace for cortical receptive field plasticity. *Nature* **450,** 425–429 (2007).

50. Klyachko, V. A. *et al.* Excitatory and Feed-Forward Inhibitory Hippocampal Synapses Work Synergistically as an Adaptive Filter of Natural Spike Trains. *PLoS Biol.* **4,** e207

(2006).

51. Bartley, A. F. & Dobrunz, L. E. Short-term plasticity regulates the excitation/inhibition ratio and the temporal window for spike integration in CA1 pyramidal cells. *Eur. J. Neurosci.* **41,** 1402–1415 (2015).

52. Tsodyks, M. V. & Markram, H. The neural code between neocortical pyramidal neurons depends on neurotransmitter release probability. *Proc. Natl. Acad. Sci.* **94,** 719–723 (1997).

53. Basu, J. *et al.* Gating of hippocampal activity, plasticity, and memory by entorhinal cortex long-range inhibition. *Science (80-.).* **351,** aaa5694-aaa5694 (2016).

54. Kim, H., Ährlund-Richter, S., Wang, X., Deisseroth, K. & Carlén, M. Prefrontal Parvalbumin Neurons in Control of Attention. *Cell* **164,** 208–218 (2016).

55. Murthy, V. N., Sejnowski, T. J. & Stevens, C. F. Heterogeneous release properties of visualized individual hippocampal synapses. *Neuron* **18,** 599–612 (1997).